



BRNO UNIVERSITY OF TECHNOLOGY

VYSOKÉ UČENÍ TECHNICKÉ V BRNĚ

FACULTY OF MECHANICAL ENGINEERING

FAKULTA STROJNÍHO INŽENÝRSTVÍ

VICTOR KAPLAN DEPT. OF FLUID ENGINEERING

EÚ-ODBOR FLUIDNÍHO INŽENÝRSTVÍ VIKTORA KAPLANA

CAVITATION COLLAPSE INDUCED BY UNSTEADY PRESSURE FIELD

KAVITAČNÍ KOLAPS VYVOLANÝ NESTACIONÁRNÍM TLAKOVÝM POLEM

DOCTORAL THESIS

DIZERTAČNÍ PRÁCE

AUTHOR

AUTOR PRÁCE

Ing. Radim Burda

SUPERVISOR

ŠKOLITEL

doc. Ing. Pavel Rudolf, Ph.D.

BRNO 2024



ABSTRACT

This doctoral thesis investigates the interaction of the cavitation structures with the unsteady pressure field induced by the cavitation collapse using experimental measurement and numerical simulations. The numerical research focuses on two case studies – the single bubble collapse near a solid wall and the hydrodynamic cavitation in the converging-diverging Venturi nozzle – to highlight the different aspects of cavitation flow on different length scales. The numerical simulations are complemented with experimental measurements conducted in the hydraulic laboratory of Viktor Kaplan Dept. of Fluid Engineering to capture the behaviour of cavitation structures in a converging-diverging Venturi nozzle. The high-speed camera recordings as well as monitoring of static pressure, dynamic pressure, radial and axial acceleration, and acoustic emission are exploited to capture the dynamics of the cavitation flow.

ABSTRAKT

Následující disertační práce se zabývá interakcí kavitačních struktur s nestacionárním tlakovým polem vyvolaným kavitačním kolapsem za použití experimentálního měření a numerických simulací. Numerický výzkum se zaměřuje na dvě případové studie – kolaps osamocené bubliny v blízkosti pevné stěny a hydrodynamickou kavitaci ve Venturiho trubici – s cílem poukázat na rozdílné aspekty kavitačního proudění na různých délkových měřítkách. Numerické simulace jsou doplněny o experimentální měření provedené v hydraulické laboratoři odboru fluidního inženýrství Viktora Kaplana s cílem zachytit chování kavitačních struktur ve Venturiho trubici. K zachycení dynamiky kavitačního proudění jsou využívány záznamy z vysokorychlostní kamery a sledování statického tlaku, dynamického tlaku, radiálního a axiálního zrychlení a akustické emise.

KEYWORDS

Cavitation, CFD, POD, single bubble collapse, Venturi nozzle, shock wave, turbulence, Ansys Fluent

KLÍČOVÁ SLOVA

Kavitace, CFD, POD, kolaps osamocené bubliny, Venturiho trubice, rázová vlna, turbulence, Ansys Fluent

BURDA, Radim. *Cavitation collapse induce by unsteady pressure field*. Brno, 2024. Doctoral thesis. Brno University of Technology, Faculty of Mechanical Engineering, Energy institute-Viktor Kaplan Dept. of Fluid Engineering. Supervisor Pavel Rudolf.



Contents

MOTIVATION AND THESIS OVERVIEW	4
1. THEORY AND APPLIED METHODS	6
1.1 CAVITATION.....	6
1.2 CAVITATION MODELLING APPROACHES	6
1.2.2 <i>Volume of fluid method</i>	7
1.2.3 <i>Euler-Euler method</i>	7
1.3 CAVITATION MASS TRANSFER MODELLING	7
1.4 TURBULENCE MODELLING	8
2 EXPERIMENTAL INVESTIGATION OF CAVITATION IN VENTURI TUBE	9
2.1 CAVITATION REGION ANALYSIS FROM HIGH-SPEED CAMERA RECORDINGS.....	9
2.2 ANALYSIS OF X-T DIAGRAMS	12
2.3 PROPER ORTHOGONAL DECOMPOSITION OF THE CAVITATING STRUCTURES.....	13
2.4 ANALYSIS OF TIME-AVERAGED SENSORS DATA	15
2.5 ANALYSIS OF DYNAMICS OF THE FLOW	16
3. CFD INVESTIGATION OF SINGLE BUBBLE COLLAPSE NEAR SOLID WALL	18
3.1 SIMULATION MODEL AND METHODOLOGY.....	18
3.2 BUBBLE COLLAPSE IN STEP-FUNCTION PRESSURE FIELD	19
3.3 EFFECT OF THE SPEED OF CHANGE OF THE DRIVING PRESSURE	21
4. CFD INVESTIGATION OF HYDRODYNAMIC CAVITATION IN VENTURI TUBE.....	22
4.1 SIMULATION MODEL AND METHODOLOGY.....	22
4.2 RESULTS OF THE CFD INVESTIGATION	23
CONCLUSION	26

Motivation and thesis overview

Temperature of the sun's surface, the pressure of deep oceanic trenches, super-sonic speed of the fastest fighter jets. We can see all of that in one single collapsing cavitation bubble. Cavitation is a complex phenomenon that appears in numerous physical and engineering flows. Common examples include turbomachinery, naval engineering, biomedical field etc. The cavitation is defined as the appearance of vapor cavities inside an initially homogenous liquid medium due to a local drop of pressure [1]. The process is commonly compared to boiling as it is also accompanied by the change of state from the liquid to the vapor phase. But in contrast to boiling where the change of state occurs due to temperature exceeding a certain level (boiling temperature), the cavitation occurs due to pressure drop below a certain level (saturated vapor pressure). The pressure in liquid can change rapidly, therefore the cavitation bubbles dynamically respond to the rapid changes by sudden growth or collapse. Cavitation bubbles in a sudden crushing high-pressure environment undergo rapid compression with violent collapse, yielding mechanical and chemical effects, most notably cavitation erosion due to the pressure shock wave, pressure fluctuation, vibrations, and acoustic and light emission.

If the cavitation bubble implosion occurs near a solid wall, the high pressure and temperature rise are capable of damaging the nearby surface. This material erosion is common for naval engineering where propellers and rudders are affected. Further examples include various types of turbomachinery (such as hydraulic turbines and pumps) [2,3], combustion applications (nozzles of injectors) [4,5], biomedical field (artificial heart valves) [6], or rocket engines [7]. Even though cavitation is usually an undesirable effect, various recent discoveries utilize the destructive nature of the cavitation bubble collapse. For instance, high intensity focused ultrasound (HIFU) exploits the destructive nature of cavitation to heat cancerous tissues and produce thermal destruction [8], the cavitation collapse is able to fragment kidney stones (shock-wave lithotripsy) [9] and fracture tissues in a non-thermal fashion (histotripsy). Cavitation is also utilized for emulsifying the natural optical lens during cataract surgery [10], for delivering drugs and targeting cells for cancer therapy [8], for precise incision in intraocular surgery [11], for fabrication of nanomaterials [12] and for surface cleaning [13]. Furthermore, as the growth environmental pollution have made the availability of safe drinking water a major problem, cavitation is effectively used for the disinfection of wastewater [14]. For more applications of cavitation see the following references [10,15].

A thorough understanding of cavitation dynamics, particularly the accurate resolution of cavitation collapse, is essential for advancements in these fields. Reliable computational fluid dynamics (CFD) simulations can significantly accelerate the design optimization process by providing rapid feedback and offering detailed insights beyond those obtained from experimental results of transient processes. The pressure and temperature inside the bubble are sufficient to ionize a small fraction of gas, creating conditions for the formation of radicals capable of undergoing chemical reactions. These radicals can react with organic compounds outside the bubble, leading to the removal of biological and chemical contaminants. Therefore, extending CFD methods to resolve cavitation collapse on the microscale of individual bubbles is beneficial to evaluate the potential for breaking chemical bonds, a challenge with current models due to the inadequate description of dispersed cavitation bubbles. The results of computational simulations and analyses of the unsteady behaviour of the cavitation cloud can be used to study the synergy between hydrodynamic cavitation and cold plasma discharge in the CaviPlasma device [27] and for predicting cavitation erosion in impellers of pumps and



turbines. This way, the simulation model can be utilized to not only predict the influence of geometry and boundary conditions changes of the device on the characteristics and dynamics of the cavitation cloud, but also its potential of removing different pollutants.

The dissertation thesis focuses its contribution on the following objectives:

- Based on the state of the art research, evaluate the potential of different modelling approaches, mainly in terms of appropriate multiphase, mass transfer and turbulence models. Additionally, underline the possibility of overcoming a challenge of inadequate description of dispersed cavitation bubbles to resolve micro-scale cavitation collapses.
- Investigate the characteristics of cavitation single bubble collapse with emphasis on the utilization of state-of-art CFD methods to underline the potential vast difference between experimentally obtained data and real hydrodynamic single bubble cavitation collapse.
- Thoroughly examine the effects of hydrodynamic single bubble cavitation collapse parameters on induced pressure waves and their impact on a solid wall, especially the effects of stand-off distance and the duration of the pressure step-function.
- Capture not only the first bubble collapse but also subsequent rebounds and assess impact pressure.
- Further the understanding of condensation shock shedding mechanism in converging-diverging Venturi tube and investigate its potential to be a pressure source for subsequent collapses.
- Examine the condensation shock pressure waves and their interaction with the cavitation structures.
- Utilize adjusted cavitation circuit of the Victor Kaplan Dept. of Fluid Engineering to capture the behaviour of cavitation structures in converging-diverging Venturi nozzle for the validation purposes of numerical models.
- Investigate the shedding mechanisms and collapse of cavitation structures by various experimental methods with emphasis on proper resolution of the subsequent pressure wave magnitude, frequency.

1. Theory and applied methods

1.1 Cavitation

The predisposition of flow to the cavitation inception is expressed by dimensionless cavitation number σ :

$$\sigma = \frac{p_{ref} - p_{vap}}{\frac{1}{2}\rho v_{ref}^2} \quad (1)$$

Where the p_{ref} and v_{ref} are determined based on investigated application. For nozzles, the reference pressure and velocity represent the upstream pressure and velocity in the throat of the nozzle. Unless the cavitation inception point is well defined (for example sharp edges of the nozzle throat), the detection of the first cavitation bubbles is rather difficult as the cavitation inception is not accompanied by the loss of efficiency or flowrate. On contrary, a slight increase in efficiency can be detected as the surface friction between the surface and surrounding flow decreases. The development of cavitation stages in the converging-diverging nozzle was experimentally investigated by Rudolf et al. [16] can be seen in Figure 1.

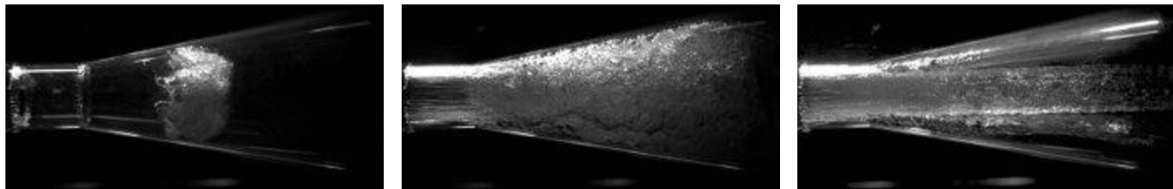


Figure 1 – Stages of cavitation (from left to right partial cavitation, fully developed cavitation, super-cavitation) [16].

1.2 Cavitation modelling approaches

Cavitation flow is basically a two-phase flow that involves mass and heat transfer between both phases. Modelling of cavitation phenomenon is a numerically challenging task as it involves concurrent treatment of two substantially distinct flow regions – the pure liquid and the vapor region. These two regions evince large differences in material properties and length scales. The pure liquid is almost incompressible whereas vapor region is highly compressible which results in high density ratio of water to vapor in the order of 10^4 and a high discrepancy of the speed of sound with a lower bound below 10 ms^{-1} and an upper bound above 10^3 ms^{-1} .

Also, the vapor fills a significantly smaller portion of the computational domain, but more importantly, the length-scale of the cavitation phenomenon ranges from small micron-scale nuclei bubbles to large meter-scale vapor cavities. Also, it is important to mention that the liquid and vapor region cannot be easily distinguished and the transition between different length-scales (for example merger of cavitation bubbles with larger cavitation cavities, break up of cavitation bubble or the growth of the bubble from small cavitation nuclei) is a numerically complex task.

The methods can be divided into the following categories: single-phase Interface Tracking Method, Volume of Fluid Method, Euler-Euler methods (multiphase, homogenous mixture) and Euler-Lagrange methods. For the purposes of this thesis, only Volume of Fluid and Homogenous mixture model is shown.

1.2.2 Volume of fluid method

The volume of fluid method, developed by Hirt and Nichols [17] in 1981, can be classified as an interface capturing method. The multiphase information of the flowing medium is represented by only one variable called volume fraction α , that describe the percentage of present phases for each cell:

$$\alpha = 0 \text{ water (phase 1); } \alpha = 1 \text{ vapor (phase 2); } 0 < \alpha < 1 \text{ interface}$$

The computational demands are decreased as only one set of equations describe the flow. Sum of the volume fractions of all phases within computational cell is equal to 1. The movement of the volume fraction (tracking of the interface between faces) is conducted by the solution of a continuity equation for the volume fraction of one or more phases. For Ansys Fluent, the equation form can be found in the following reference [18].

The VoF method is usually used for simulations of free surface flow where the interface between phases can be easily tracked, but it can also be valuable for simulations of sheet cavitation, single bubble motion and cavitation bubble collapse, where precise interface is needed. However, this method fails to describe structures that are smaller than the grid size which means it is not able to describe large number of small cavitation bubbles which influence the global dynamic of the flow (for example cloud cavitation).

1.2.3 Euler-Euler method

For various types of cavitating flow, the flow contains large number of small, dispersed bubbles so the precise location and properties, and therefore interfaces between phases, are not clearly apparent of the global scale. This problem can be overcome by averaging techniques where the bubbles are considered collectively as the equivalent continuum mixture [19]. The homogenous mixture models use averaging to obtain single pseudo-fluid with averaged properties resulting in the treatment of the whole domain as a compressible fluid with vastly varying density. Both cavitating and non-cavitating region therefore share the same pressure, velocity and temperature fields. To compute the density field two common strategies are used – equation of state (EoS) or volume fraction transport equation [20].

The second option is to solve the volume fraction transport equation (TEM) to account for the mass transfer rate between the water and the vapor phase by adding an appropriate source term. The main advantage of this method is that the dependency of the mass transfer on time can be considered by empirical law for the source term.

1.3 Cavitation mass transfer modelling

As mentioned, the modelling methods have to be expanded to account for mass transfer between the liquid and the vapor via vapor transport equation (TEM):

$$\frac{\partial}{\partial t}(\alpha_{vap}\rho_{vap}) + \frac{\partial}{\partial x_j}(\alpha_{vap}\rho_{vap}\bar{v}_{vapj}) = R_e - R_c \quad (2)$$

Where the terms R_e (evaporation of the liquid) and R_c (condensation of the vapor) account for the mass transfer between the liquid and vapor phases in cavitation. The Schnerr and Sauer model [21] derives the exact expressions for the net mass transfer from liquid to vapor. The most important feature of this model is the resolution of the interior disperse structure of the bubble cloud. Due to modelling of the nuclei content, it is possible to reconstruct the number

of bubbles in the cell and their radii from the vapor content of the cell. Therefore, the Schnerr and Sauer cavitation model connects the vapor volume fraction to the number of bubbles per volume of fluid by the following equation:

$$\alpha_{vap} = \frac{n_0 \frac{4}{3} \pi r_B^3}{1 + n_0 \frac{4}{3} \pi r_B^3} \quad (3)$$

From the equations, we can see that the only parameter that needs to be determined is the bubble number density n_0 . The bubble density is coupled to the volume of liquid not to the volume of the mixture. This approach allows to conserve the number of bubbles and the parameter can be therefore utilize for various stages of bubble lifetime.

1.4 Turbulence modelling

The majority of cavitation occurrences entail turbulence, but the interaction between turbulence and cavitation is insufficiently documented phenomenon, because of challenges associated with conducting experimental measurements within cavitating fluid regimes. Furthermore, the impacts of compressibility on turbulence and the influences of the dispersed phase remain largely uncharted. The precise numerical precision in simulating turbulent cavitation hinges on the comprehensive modelling of both cavitation and turbulence. Consequently, the selection of an appropriate turbulence modelling approach is a critical subject [22].

To improve the turbulence modelling and to try to better simulate the re-entrant jet behaviour and the vapor cloud shedding, Coutier-Delgosha et al. [23] modified the standard k- ϵ model simply by reducing the mixture turbulent viscosity, particularly in regions characterized by low volume fraction. This proposed formula can also be adapted for k- ω models in the following manner:

$$\mu_t = f(\rho_m) \frac{k}{\omega}; f(\rho_m) = \rho_v \frac{(\rho_m - \rho_v)^{n_0}}{(\rho_l - \rho_v)^{n_0 - 1}}; n_0 > 1 \quad (4)$$

When applied to cavitating flow, the utilization of ρ_m noticeably decreases turbulent viscosity in regions of the flow with a high vapor volume fraction. Conversely, for non-cavitating liquid flow, the formula for μ_t remains consistent with its original form. In this study, the exponent n_0 was set to 10, and the representation of this modification can be observed in Figure 2 . We can clearly see the decrease of turbulent viscosity in the area of cavitation structures.

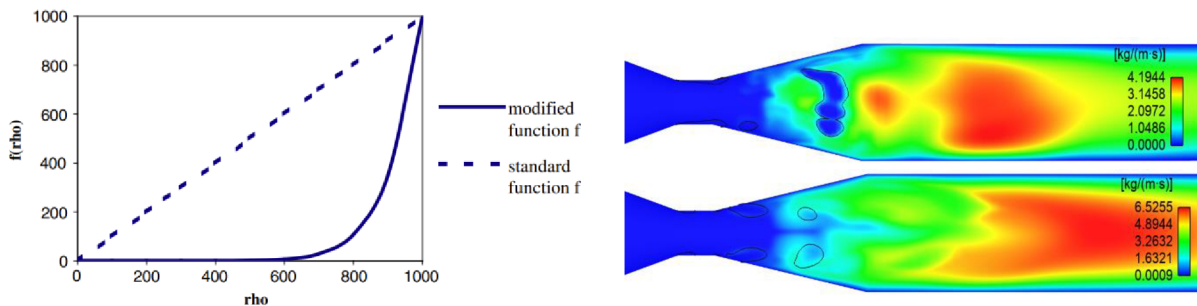


Figure 2 – Left Modification of the mixture turbulent viscosity ($n_0 = 10$) [23]., Right Comparison of turbulent viscosity for SST with modified turbulent viscosity (top) and standard SST (bottom)

While RANS modelling proves highly valuable, it falls short in capturing disturbances initiated by local flow instabilities, such as cavitation shedding behaviour. Therefore, Scale Resolving approach such as SBES [24] can be beneficial to correctly predict shedding behaviour and

resulting unsteady pressure fluctuations. SBES model uses a RANS model for near wall flows and Large Eddy Simulation (LES) for the large, detached flows. Existing RANS and LES models are ‘blended’ by a shielding (or blending) function. While the formulation is seemingly simple, its complexity is concentrated in the shielding function. The SBES uses strong shielding function for the RANS region which results in faster transition between RANS and LES regions, leading to lower eddy viscosity and more resolved turbulence. Furthermore, SBES allows for all combinations of all RANS and all (algebraic) LES models and remain robust even on non-perfect industrial meshes [24].

2 Experimental investigation of cavitation in Venturi tube

2.1 Cavitation region analysis from high-speed camera recordings

An experimental measurement is conducted in the hydraulic laboratory of Viktor Kaplan Dept. of Fluid Engineering to capture the behaviour of cavitation structures in converging-diverging Venturi nozzle for the validation purposes of numerical models. For the experimental measurements, the cavitation circuit is utilized (the schematic can be seen in Figure 3). Water is supplied by a pump controlled via a frequency converter, which ensures comfortable adjustment of flow rate over a relatively wide range. The level of static pressure within the circuit is modified by a vacuum pump or pressurized air injection above the water level in the pressure vessel. The combination of flow rate and static pressure control enables the operation of the circuit from no cavitation regime to full super-cavitation. The experimental circuit is mounted with static pressure sensors, dynamic pressure sensors, radial and axial accelerometers, and acoustic emission sensors. Also, during all the measurements the high frame-rate camera was present to obtain dynamics from the image analysis. The circuit was extended with see-through piping behind the inception points in the Venturi nozzle, which allowed us to investigate the super-cavitation region more thoroughly.

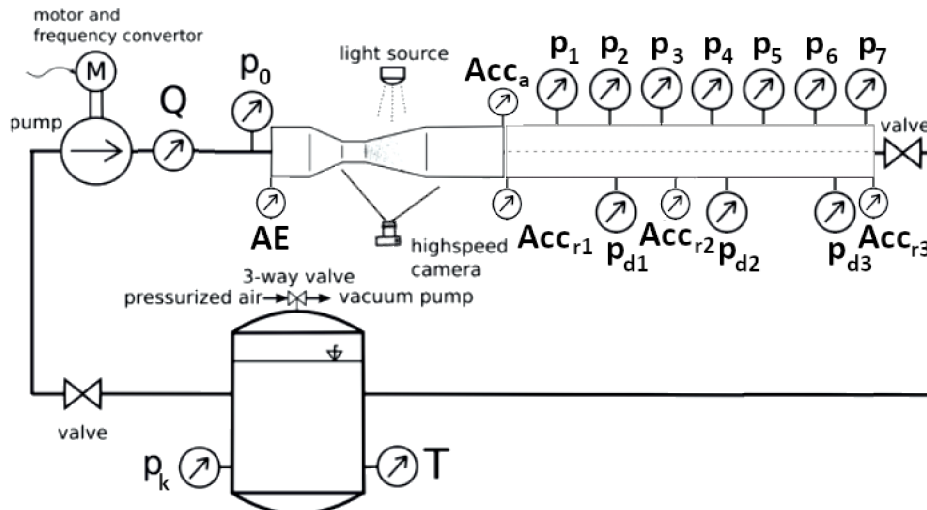


Figure 3– Scheme of cavitation circuit.

To more efficiently discuss the cavitation structures for different configurations of flow rates and operating pressure in the tank, the whole range of cavitation numbers is divided into regions with characteristic cavitation structures. To better understand the differences between regions, the averaged RMS results of pressure pulsation from dynamic Kistler sensor are used (Figure 4). Only the final results are compared for the different flow rates that range from 4 l/s to 7 l/s.

It should be also noted that the definitions for different regions of cavitation are not clear and universal in the literature and the transition regions can be subjective.

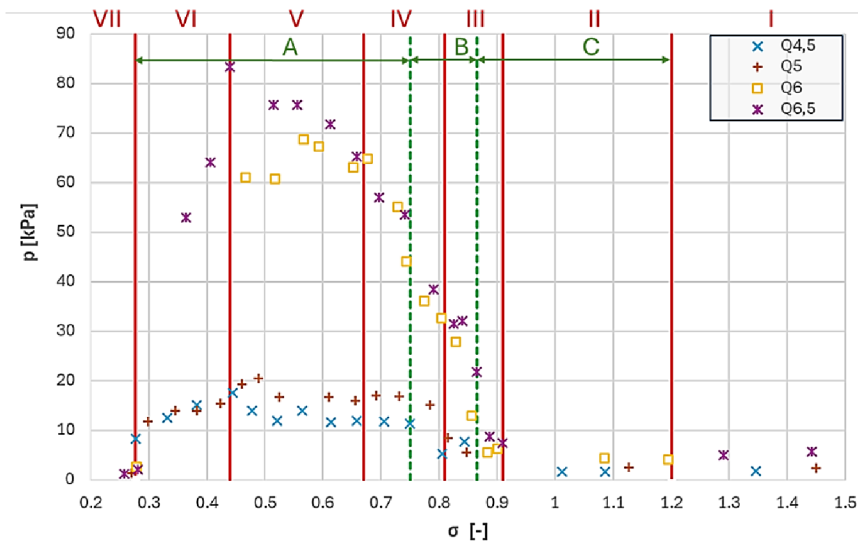


Figure 4 – Division of cavitation regions based on RMS values of pressure pulsation from dynamic Kistler pressure sensors.

The range of cavitation numbers was divided into the following regions: I. No cavitation, II. Cavitation occurs only on defects in the Venturi tube, III. Initial cavitation, IV. Partial cavitation, V. Fully developed cavitation, VI. Fully developed cavitation – transition to super-cavitation, VII. Super- cavitation. Also, the regions are divided based on the dominant mechanism responsible for cavitation shedding: A. Re-entrant jet, B. Transition region, C. Bubbly-shock mechanism.

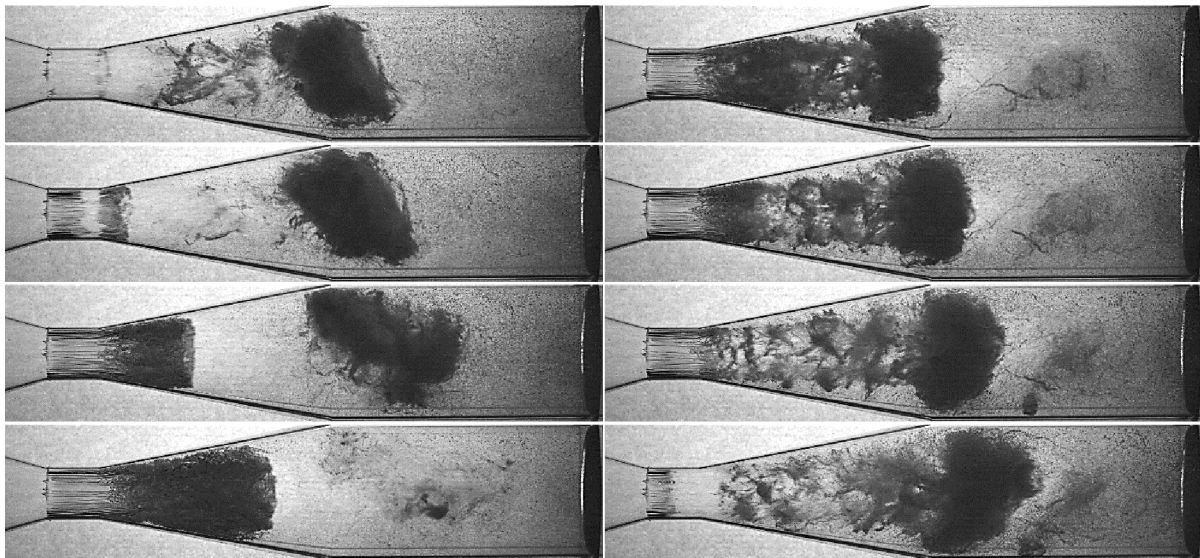


Figure 5 - Fully developed cavitation ($Q4.5$; $\sigma 0.48$).

While it is beneficial to study the raw images from high-speed cameras recording, more thorough analysis of emerging mechanisms can be obtained from spatially and temporally averaged images. Thus, Python script was created to automatize the analysis. In Figure 5, we can see an example of cavitation shedding cycle for the fully developed cavitation. The Python Imaging Library was utilized to extract image intensities. The saved arrays of greyscale pixel intensities range from 0 to 255. Also, the script is utilized to crop the images to specify analysed

area and retrieves information about the images that are then used to automatically find corresponding record from all sensors used during the experiment. The data from the sensors are used to determine flow rate and cavitation number so the statistical analysis of different experimental setups can be automatically compared.

To get comprehensive information about the length and the amount of domain occupied by the vapor phase that can be presented in single plot for various cavitation numbers, the mean time-averaged images are used. Similarly, to acquire a better understanding of the fluctuations of cavitation structures, the standard deviation of the time-averaged images can be exploited. The time-averaged images are almost uniform in the vertical direction and therefore the important information can be condensed into 1-D curves by spatially averaging in this direction. The results are charts of averaged pixel intensity as a function of x-coordinates over all cavitation numbers. To see the results more clearly, the 1-D curves are represented in 2-D plots. The 2D plot is divided into regions based on cavitation number (white lines), dominant shedding mechanism (red line; a – transition region, b – bubbly shock mechanism) and transition parts of Venturi nozzle (black lines).

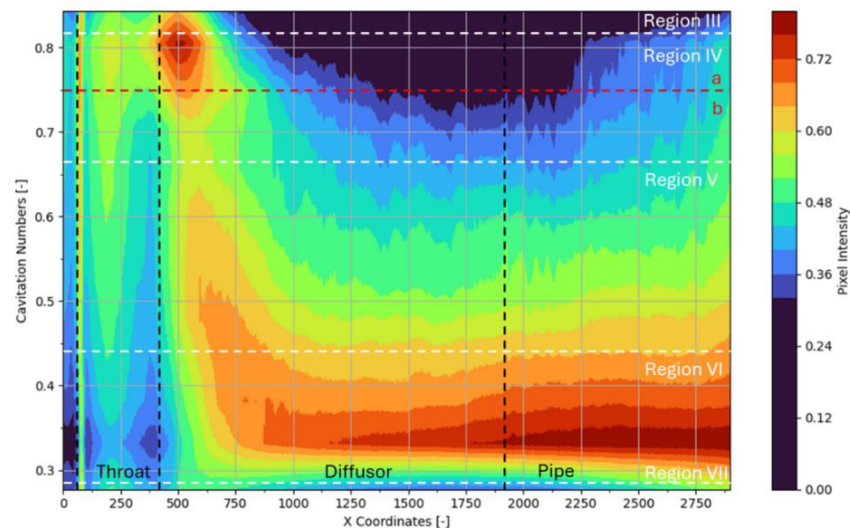


Figure 6 – 2-D plot of time-averaged normalized pixel intensity for the full range of cavitation numbers ($Q4.5$).

From the Figure 6, we can clearly see the inception region on the leading and trailing edge of the Venturi where sudden rise of normalized pixel intensity occurs. Up until the transition to bubbly shock dominant shedding mechanism we can see a stable region around the trailing edge of the throat. This stable region completely decays once the pressure wave from the bubble collapse is strong enough to decay the entire cavitation structure. This can be also observed from sudden decrease of the normalized pixel intensity in the throat. We can also see the transition from partial cavitation to the fully developed cavitation as the normalized pixel intensity starts to increase more rapidly with decreasing cavitation number. The region of transition to super-cavitation and super-cavitation region can also be distinguished as the normalized pixel intensity starts to progressively decrease from trailing edge of the throat which, as stated earlier, corresponds to the lower number of interfaces between bubbles and continuous fluid as the cavitation structures become more uniform. The drop in normalized pixel intensity advances to the whole domain around $\sigma = 0.3$ which indicates full transition to super-cavitation. As the 2-D plots for various flow rates show similar behaviour, it can be determined that the flow rate does not influence the dependency on cavitation numbers.

2.2 Analysis of x-t diagrams

Another approach to describe the dynamics of the global cavitation characteristics is to spatially average the pixel intensities along the y-axis without time-averaging. The result is the single line of data along the x-axis that represents the instantaneous overall shape of the cavitation structure which means that it cannot be used to capture localized instabilities or non-axisymmetric structures. By stacking these lines through the whole captured time interval, an x-t diagram is created. The x-t diagram can be used not only to determine the cavity length similarly to the 2D maps of time and space averaged values and standard deviation of pixel intensity, but also to determine the mechanism of cavitation shedding and frequency of the shedding cycle. To get a finer resolution, the recording of only the halved domain is used that benefits from higher framerate of the camera.

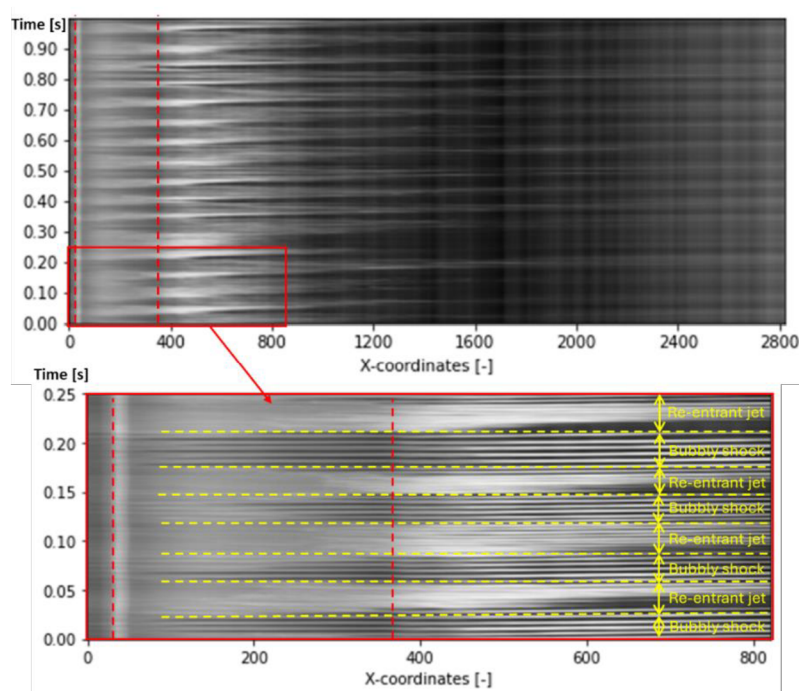


Figure 7 - x-t diagram, showing cavitation dynamics, for the whole domain (top) and for detailed section (bottom) for Q6.5, $\sigma 0.86$ (the dotted red line represents the throat of the Venturi nozzle).

In Figure 7, we can see the transition region (Q6.5, $\sigma 0.865$), where both shedding mechanisms take place. The white regions of cavitation clouds transition quickly to black colour that indicates pressure wave decaying the cavitation cloud. As described before, the mechanism appears in “bundles”, where, if the pressure wave from the cavitation collapse is sufficient enough to decay the entire cavitation structure, the following emerging cavitation structure is big enough to create a sufficient pressure wave. Once a smaller cavitation vortex ring is shed that is not sufficient to decay the entire structure, the re-entrant jet starts to be dominant and results in more frequent shedding with smaller cavitation structures that cannot decay the entire cloud. With decreasing cavitation number, the cavitation structure size increases and therefore the bubbly shock mechanism is more dominant. The re-entrant jet operates on smaller length and time scale.

In the detail, we can see that the cavitation cycles and transitions between both mechanisms are apparent even with low framerate. The recording starts in the bubbly shock region. We can see 3 collapses that decay the entire structure. Only a small cavitation cloud is then shed and

therefore the resulting pressure wave sheds even smaller structure. The dominant mechanism changes to re-entrant jet. Around 0.6 s the dominant mechanism changes back to bubbly shock mechanism. From the recorded images we can observe that large cavitation cloud is being shed by the re-entrant jet mechanism. The resulting pressure waves sheds progressively larger structures and therefore the dominant mechanism changes again.

To determine the frequency of the shedding the FFT analysis of the temporal direction is performed. The intensity fluctuations record in specified cross-section of the domain can be quickly determined from x-t diagram by taking only the vertical direction in specified x-coordinates and thus creating course plot of averaged pixel fluctuations as a function of time. In Figure 8, we can see the comparison of the first dominant frequency for the whole range of cavitation numbers for various flow rates. We can clearly see that all flow rates follow the same pattern of decreasing dominant frequency with decreasing value of σ , which corresponds to the increase in compliance of the medium with higher vapor phase content. The frequencies are slightly higher for higher flow rate and, as previously stated, the transition between re-entrant jet and transition region also varies slightly with different flow rate. The results will be compared to the sensors analysis and frequencies from POD in later chapters.

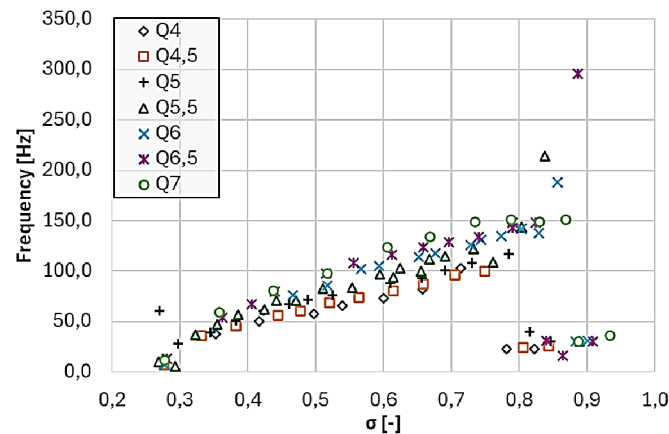


Figure 8 - Comparison of the 1st dominant frequency for the whole range of cavitation numbers for various flow rates.

2.3 Proper orthogonal decomposition of the cavitating structures

This section provides a brief overview of the fundamental principles and main processes involved in Proper Orthogonal Decomposition (POD) for visualizing coherent structures within fluid flows. For more thorough description of the POD method, see [25]. POD serves as a general spatial-temporal framework functioning as a reduced-order model in fluid dynamics applications. It is commonly utilized for investigating coherent turbulent structures but can be utilized for the purpose of cavitation flow dynamics by processing the pixel intensities from the high-speed camera recordings. Firstly, the spatial modes are analysed for various cavitation numbers and flow rates and then the corresponding frequencies of the most dominant modes are determined based on FFT analysis of temporal decomposition.

In Figure 9, the 1st spatial modes for the whole range of cavitation numbers are depicted. From the images, it can be determined the most energy is contained in the axial pulsation of the cavitation cloud. The length of the spatial mode region follows similar pattern as the length of cavitation structures – with decreasing σ , the length increases. Also, the region with dominant re-entrant jet shedding mechanism can be distinguished from the transition region by observing the throat area of the Venturi nozzle. From the analysis of pixel intensities, we located stable

region on the trailing edge of the nozzle because the shedding mechanism was unable to propagate to the leading edge and decay the entire cavitation structure.

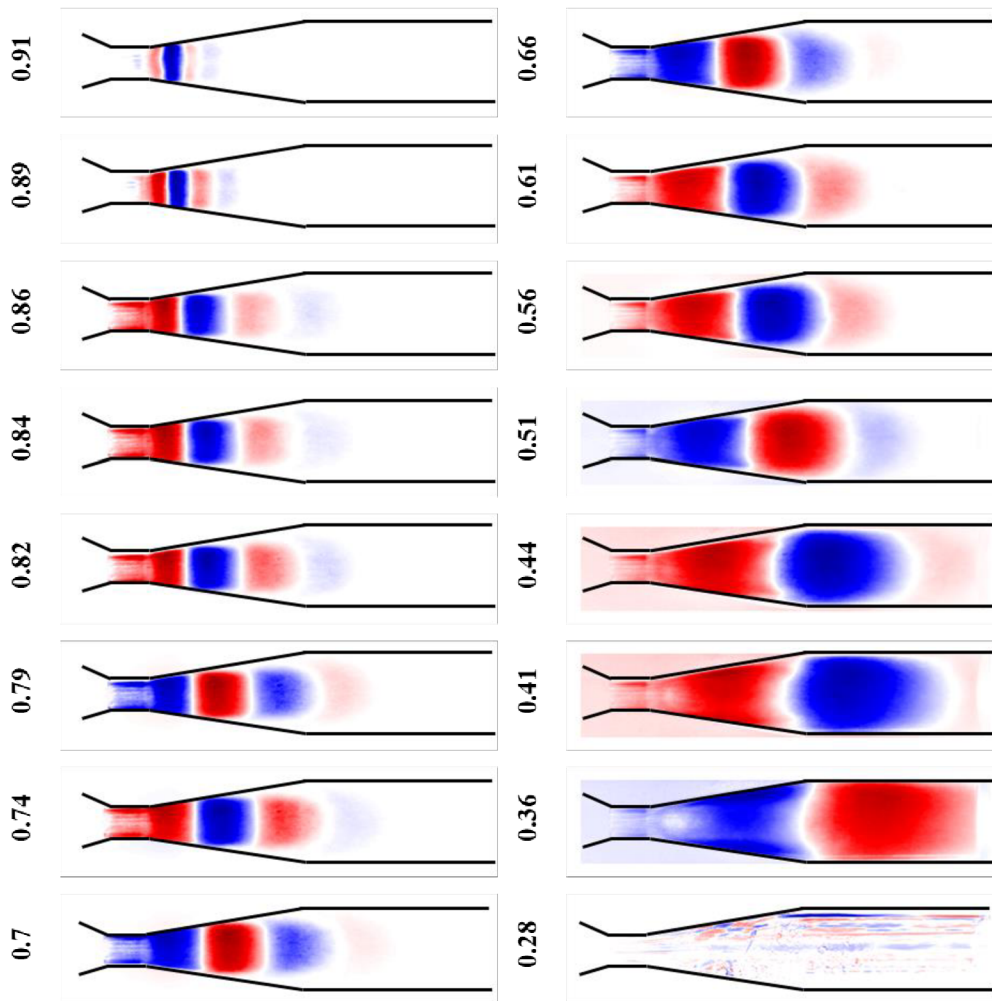


Figure 9 – Comparison of the full range of cavitation numbers (Q6.5)

In Figure 10, we can see the x-t diagram and 4th and 5th spatial and temporal mode for $\sigma = 0.86$, which is region where both shedding mechanisms can be identified. The most dominant frequency is 16 Hz which is connected to the switching between mechanisms. This is confirmed by the x-t diagram where we can clearly see 16 transitions between re-entrant and bubbly shock mechanism. The spatial mode also confirms this as we can see oscillation between two un-even structures. The importance of the “switching” frequency is highest in the middle of the transition region and decreases once one of the shedding mechanisms is prevalent.

In the Figure 11, we can see comparison of the frequencies of the first 6 mode in the whole range of σ for the Q 6.5 l/s. Corresponding mode pairs can clearly be identified for the most of the σ range for the first 4 modes. The first 4 modes also correspond to the dominant and first harmonic frequency for most of the analysed range. The only exception is the region of partial cavitation with transition between shedding mechanisms. Also, for the end stage of fully developed cavitation we can see that the 5th and 6th mode create pair that corresponds the second harmonic of the fundamental frequency. In Figure 11, we can also see the dominant frequencies of the 1st mode as a function of flow rate. We can see that the courses of the frequencies are not influenced by flow rates for most of the cavitation number range. The frequency amplitude

increases with increasing flow rate. As was previously stated, the flow rates start to influence the cavitation behaviour in the transition region where for the higher flow rates the dominant frequency is connected to the bubbly shock mechanism even for higher values of σ before rapidly decreasing to the low frequency connected to the “switching” mechanism.

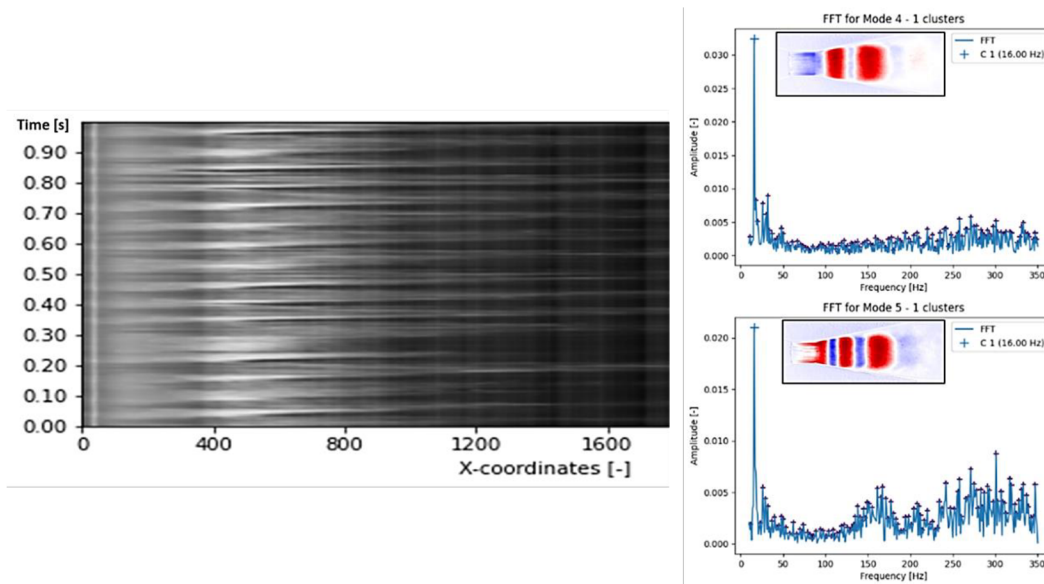


Figure 10 – Comparison between $x-t$ diagram and mode decomposition in the transition region of shedding mechanisms ($\sigma 0.86$)

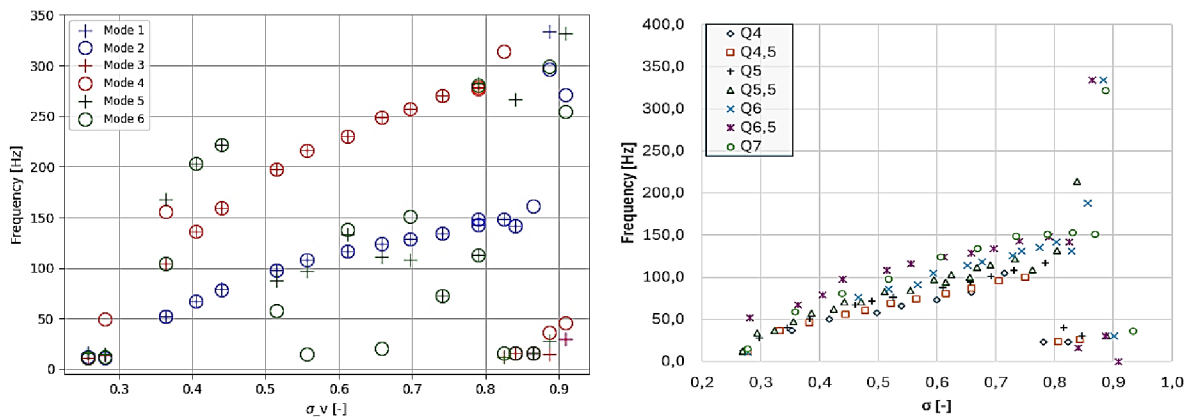


Figure 11 – Left: Dominant frequency of the first 6 modes for the whole range of σ (Q6.5); Right: Dominant frequency of the 1st mode for the whole range of σ and flow rates.

2.4 Analysis of time-averaged sensors data

The following chapter describes analysis of recorded signal from all transducers used during cavitation experimental measurements. In Figure 12, we can see the hydraulic loss coefficient for all experimental configurations. The loss coefficient is calculated by equation 5. In the chart, we can see the same constant loss coefficient for non-cavitation region for all flow rates. When the cavitation starts to emerge on the defect in Venturi nozzle, we can see small decrease of loss coefficient as the vapor surrounds the walls and decreases the friction. Once the partial cavitation is present the loss coefficient increases with decreasing σ linearly for all configurations. A small effect of flow rate can be observed in increase of loss coefficient with increasing flow rate. It should be noted that the precise decrease in loss coefficient in the region

of cavitation inception is very sensitive due to sudden change in flowrate and dependency whether the pressure in the system is increased or decreased to this point by vacuum pump.

$$\xi = \frac{p_0 - p_7}{0.5\rho v_t^2} \quad (5)$$

In Figure 13, we can see the RMS and rolling maximum values for the first Kistler sensor for the whole range of σ and Q . The pressure pulses do not increase linearly up until transition to super-cavitation, but similarly to radial pulsations decrease slightly with the transition from partial to fully developed cavitation and increase again up until transition to super-cavitation. This development can be observed with all flow rate values with differences of the specific value of σ where the transition occurs. From the absolute values of RMS, we can also detect non-linear increase with increasing flow rate. The RMS value for $Q = 4\text{-}5$ l/s and $Q = 6\text{-}7$ l/s create two bundles of similar values with $Q = 5.5$ l/s in the transition region.

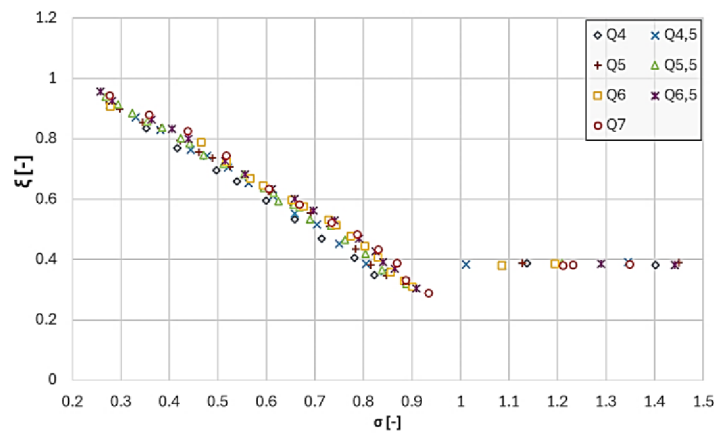


Figure 12 – Hydraulic loss coefficients for the full range of σ and Q .

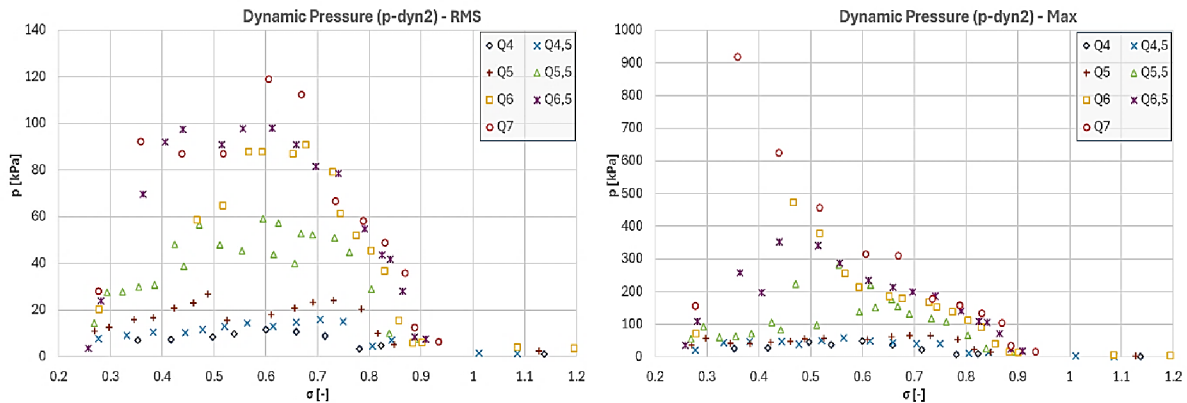


Figure 13 - RMS and rolling maximum values of Kistler pressure records for the whole range of σ and Q .

2.5 Analysis of dynamics of the flow

In the following chapter the character of the cavitation dynamics is observed by evaluation of raw transducers signal and FFT analysis. The results are then compared to the POD and pixel analysis of the dominant frequencies. The evaluation is performed with flow rate of 6.5 l/s and because of the vast number of studies configurations, only key plots are shown to highlight most important aspects of the emerging dynamics.

In Figure 14, the comparison of dominant frequencies from pressure and accelerometer sensors for the whole range of σ is shown. In the left plot, we can see a flow rate of 4.5 l/s and in the right plot the flow rate of 6.5 l/s. The accelerometer 3 and transducer of acoustic emission are not shown for the $Q = 6.5$ l/s due to oversaturation. The frequencies were determined by a semi-automatic method where during post-processing the local maxima are determined by k-means clustering. While this method showed reasonable accuracy for the pressure signal, it was difficult to utilize for the noisier signal from the accelerometer. Therefore, manual supervision had to be employed to resolve problematic regions.

For the higher flow rate, the dominant frequency from all sensors is in reasonably good agreement. The most dominant bubbly-shock mechanism is present in nearly the whole range apart from $\sigma = 0.91$ and 0.89. Similar uniformity of all sensors can be applied to higher measured flow rates between 6-7 l/s. For lower flow rates the signal becomes noisier and therefore the determination of dominant frequency is less clear. When we look at the dependency for $Q = 4.5$ l/s, we can see that the pressure signals are once again in agreement, but comparison with accelerometers is less uniform. The frequency of the axial pulsations follows the trend of pressure pulsation, except for the unstable re-entrant jet to bubbly mechanism transition and transition to super-cavitation.

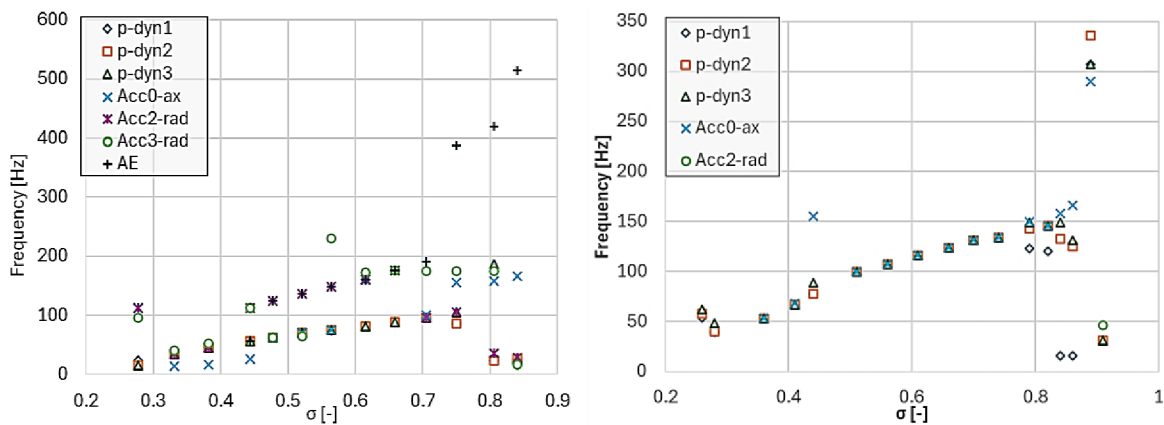


Figure 14 - Comparison of dominant frequencies from pressure and accelerometers sensors for the whole range of σ (left $Q4.5$, right $Q6.5$)

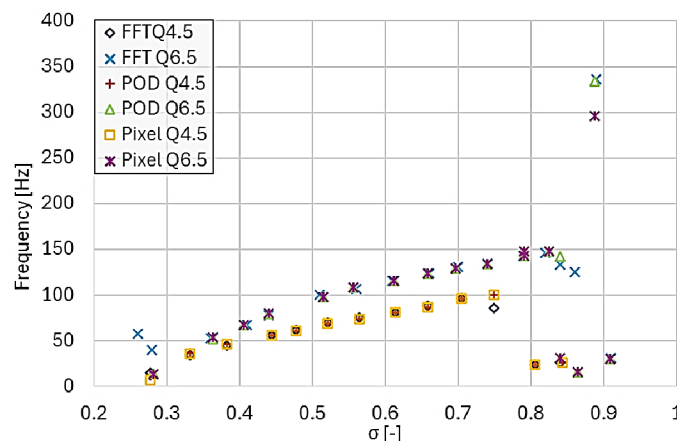


Figure 15 - Comparison of most prevalent frequency from the POD, $x-t$ diagram and FFT analysis of p_{d2} for $Q4.5$ and $Q6.5$.

In Figure 15, the comparison of the frequency of the first mode, the dominant frequency from the pixel $x-t$ diagram and the dominant frequency from FFT analysis of pressure signal p_{d2} can



be observed for $Q = 4.5$ l/s and $Q = 6.5$ l/s. The results from all methods are in agreement for the whole cavitation range. The only discrepancy is in the transition region of partial cavitation where the signal is noisier and therefore identification of the dominant frequency can be problematic. Both FFT and POD methods are able to show the transition to the high-frequency region of the re-entrant jet before rapidly declining to a low frequency of around 30 Hz. Also, in contrast to frequencies from the x - t diagram, both the FFT and POD methods are in agreement with the frequency of the re-entrant jet mechanism. The benefit of determination from pressure signal is that the super-cavitation region can be studied as well, whereas no relevant data can be used from high-speed camera record as the region appears to be stable and no effect of occasional pressure waves can be seen. All methods show the dependency on flow rate where higher flow rates result in an increase of prevalence frequency as well as a quicker transition to the bubbly-shock shedding mechanism.

3. CFD investigation of single bubble collapse near solid wall

3.1 Simulation model and methodology

The precise flow measurements are complicated to obtain experimentally due to small spatial and time scales. Therefore, numerical simulations emerged to complement the analytical and experimental analysis and further deepen our understanding of the cavitation phenomenon. Only in recent years the inclusion of the bubble growth phase (energy deposit) has started to emerge which was shown to have a huge impact on the resulting development of the collapse as it introduces asphericity in earlier stages of the collapse. The most common approach is to mimic laser-induced cavitation because it can be easily verified by the experiment, but this type of collapse does not correspond to the hydrodynamic energy deposited collapse, which most commonly occurs in engineering applications due to high-pressure gradients near solid surfaces. As mentioned before, to our knowledge, only Hsiao et al. [26] were able to simulate this type of energy-deposit collapse. The sudden sharp rise of pressure results in higher magnitudes of impact pressure and velocity during the collapse. Specifically, jet velocities exceed the speed of sound (the peak value of 1600 m/s) and impact pressures are in the range of GPa. Therefore, in order to properly assess the impacting pressure waves, this type of energy-deposited boundary conditions must be used, even though this setup is numerically challenging.

Based on the findings from state of the art, two simulation cases are presented for the single bubble collapse near the solid wall – the collapse in periodic pressure field and more challenging hydrodynamic energy deposited collapse with sudden pressure rise. The collapse in the periodic pressure field is used to assess the validity of proposed simulation methods. Only the results from the step-function pressure boundary conditions case are presented here.

The simulation model and methodology are kept very similar for both simulation cases. The bubble collapse near the solid wall is simulated using axisymmetric calculation (see Figure 16). The domain is spatially discretized by fully structural hexahedral cells and locally refined in the vicinity of the bubble and solid wall. The resulting mesh count is between 250 000 - 400 000 elements with a cell size of around 0.7 nm in the area of interest.

The bubble is subjected to an external pressure field which is driven by pressure boundary conditions on the edge of the liquid domain. The pressure step function for the second case is described by equation 24. The initial pressure is atmospheric and after 10 μ s the imposed pressure is dropped to 10 000 Pa to initiate bubble growth that introduces asphericity to the

simulation due to proximity of the wall. After 15 μs , the imposed pressure linearly rises again to the specified value p_p with a prescribed duration of t_s .

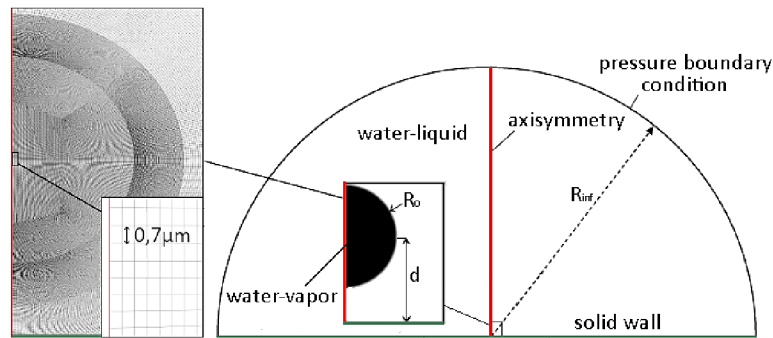


Figure 16 - Liquid domain with detail of quadrilateral mesh near solid wall.

$$\begin{aligned} t < 10 \mu\text{s}: p &= 101\,325 \text{ Pa} \\ 10 \mu\text{s} < t < 25 \mu\text{s}: p &= 10\,000 \text{ Pa} \\ t > 25 \mu\text{s}: p &= p_p(t_s) \end{aligned} \quad (6)$$

3.2 Bubble collapse in step-function pressure field

In Figure 17, we can see the evolution of bubble collapse for $\gamma = 0.5$ and $p_d = 5 \text{ MPa}$. In image 1 we can see the aspherical growth due to close proximity to the wall. We can see microjet intrusion and collapse. The microjet pressure wave impacts the wall with a pressure magnitude of around 1.8 GPa, while the pressure right after the jet penetration is up to 5.6 GPa. The bubble starts to split on the surface close to the wall right after the microjet penetration. The bubble splits after the impact of the microjet on the solid wall and the resulting ring follows the liquid jet towards the wall and then propagates outwards of the centre and collapses during the second rebound phase (not depicted here).

Just before the bubble collapse, the bubble splits again creating a second split ring. After the collapse of the bubble, the resulting pressure wave of 6.6 GPa is propagated towards the solid wall. Before the impact, the second split ring collapses creating another pressure wave of almost 7 GPa that interacts with the pressure wave from the original bubble collapse and reversed microjet impact. Both waves impact the wall in quick succession, with a first impact of 2.7 GPa from the original bubble structure and 3.3 GPa from the second bubble ring. In the location of the collapse of the secondary ring, we can observe a quick rebound as another cavitation ring starts to enlarge. This third cavitation ring flows close to the solid wall where another collapse occurs impacting the wall with a pressure magnitude of 2.1 GPa.

The evolution of pressure impact on solid wall and R_{eq} for the mentioned configuration can be seen in Figure 18. We can clearly see 4 peaks of pressure impact on the solid wall. The first corresponds to microjet impact, the second to the collapse of the second split bubble structure, the third to the collapse of the main bubble and the fourth to the collapse of the third split bubble structure. The magnitude of all pressure peaks increases with increasing driving pressure p_d . The timing of the main and the second split bubble structure collapses coincide with each other and create only one pressure peak for $p_d = 1 \text{ MPa}$ which results in an even larger impact than for $p_d = 2.5 \text{ MPa}$. The resulting pressure wave also influences the collapse of the third split bubble structure where only a small rise in pressure can be monitored on the solid wall. This can be also seen from the evolution of R_{eq} , where the usual two changes of trend that corresponds to the collapses of main and second split bubble structures, cannot be observed.

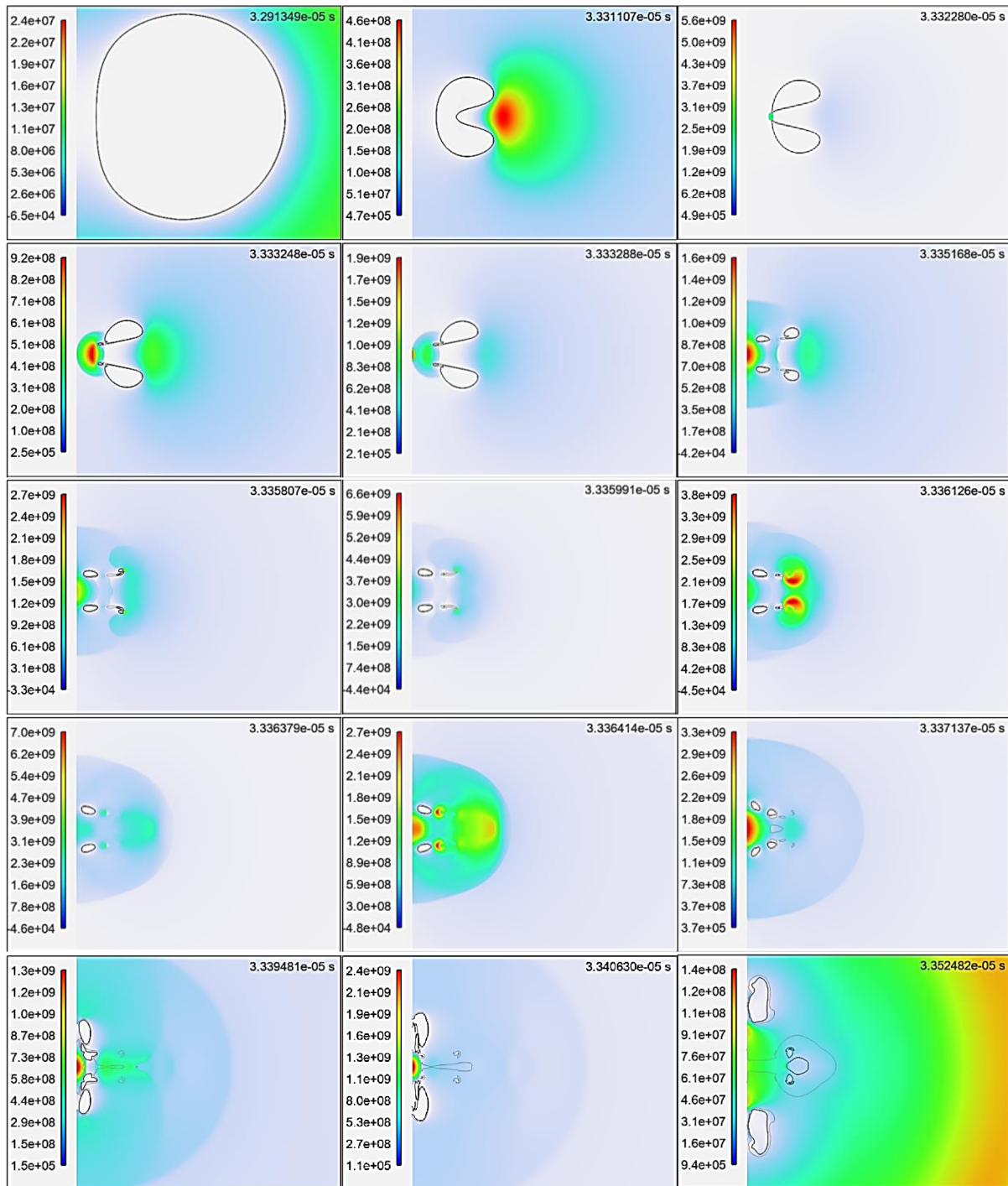


Figure 17 - Pressure contours at different stage of bubble collapse near solid wall (solid wall is on the left side of every picture) for $\gamma = 0.5$, $p_d = 5\text{MPa}$. The black and grey line correspond to volume fraction iso-surface of 0.5 and 0.1, respectively. From left to right: 1. Aspherical growth of the bubble, 2. start of the microjet intrusion, 3. microjet right after the impact, 4. bubble splitting at the surface close to solid wall, 5. microjet impact on solid wall, 6. progression of collapse of the original bubble and growth of the split part of the bubble, 7. second splitting of the bubble right before the collapse, 8. bubble collapse, 9. focus of the pressure wave in direction towards solid wall, 10. collapse of the second split part of the bubble, 11. focus of the emerging pressure wave towards solid wall, 12. growth of rebound structure from the second split of the bubble, 13. splitting and start of the collapse of the rebounded structure 14. collapse and impact of the rebounded structure on the solid wall, 15. propagation of the first split part of the bubble outwards of the centre.

The second image shows the comparison of pressure impact magnitude of the most significant phenomena for $p_d = 5\text{MPa}$ and for various γ . Please note that only one pressure peak is present for $\gamma = 1$ which is listed as the impact of the main bubble collapse but is associated with jet

penetration as well. The dependency confirms rapid exponential growth for the impact of the main and second bubble structure whereas the growth for jet penetration is almost linear for both configurations. The impact from the third structure collapse also shows exponential growth but with a smaller magnitude and change in trajectory. The change in p_d also seems to influence the steepness of the growth and not only offset, but the influence is much lower than for the stand-off distance.

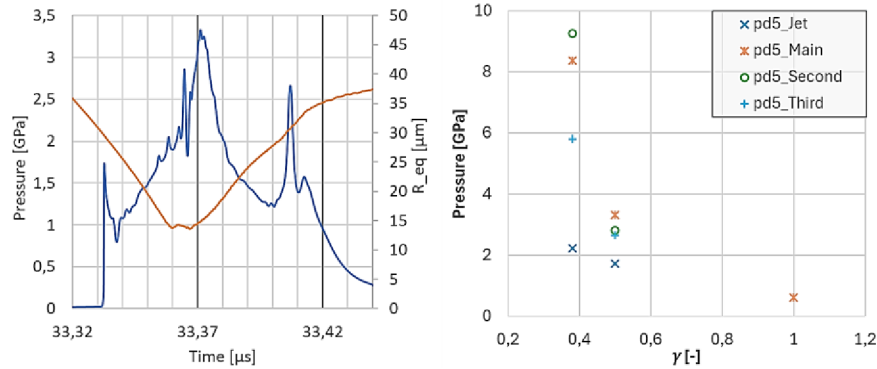


Figure 18 - Evolution of pressure impact on solid wall and equivalent radius in time for $\gamma = 0.5$ and all configurations of driving pressure p_d (from left to right 5)

3.3 Effect of the speed of change of the driving pressure

In previous the chapter, we utilized an infinitely small duration of the step change of pressure on boundary condition, as it more closely matches the situation of high-pressure gradients near solid walls (for example on the suction side of the impeller). In reality, the change is not infinitely small so a new parameter – the duration of the step-function t_s is introduced. This parameter describes the time in which pressure boundary conditions change from bubble growth phase pressure to the driving pressure p_d . The simulations are conducted and for $\gamma = 0.5$ and $p_d = 5$ MPa, as it provides interesting interactions between pressure waves from collapsing split bubble structures as well as super-sonic velocity during the jet penetration. The simulations are performed for t_s values of 4, 6 and 8 μs .

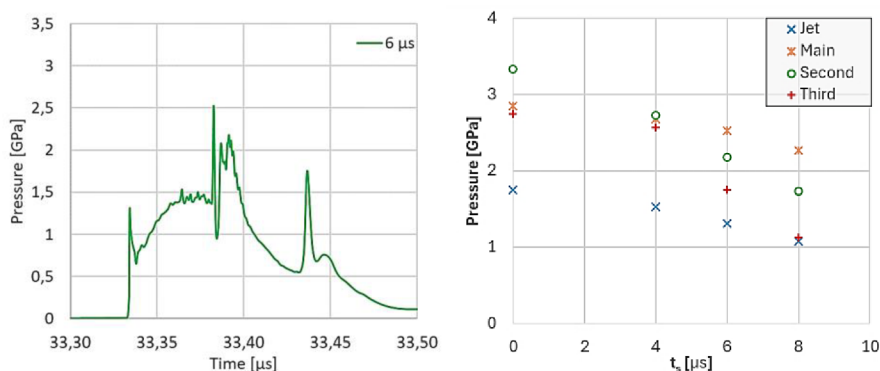


Figure 19 – Evolution of pressure impact on solid wall for $\gamma = 0.5$, $p_d = 5$ MPa, $t_s = 6 \mu\text{s}$ (left), Comparison of the most significant pressure impact peaks for variable t_s (right)

In Figure 19, we can see the evolution of pressure impact on solid wall for $t_s = 6 \mu\text{s}$ and the comparison of the most significant pressure impact peaks for variable t_s . The nature of the pressure impact remains the same for all simulated configurations as all the most distinct pressure peaks all present (from the jet penetration, main bubble collapse and second a third split bubble structure collapse). As expected, the magnitude of all pressure impacts decreases

with increasing t_s . Interestingly, the significance of the impact of the second split bubble structure decreases with increasing t_s . We can see that for $t_s = 0 \mu\text{s}$, the magnitude is even greater than for the main bubble collapse. For $t_s = 4 \mu\text{s}$, the magnitudes are comparable and for lower values of t_s the main bubble collapse starts to be more significant. During the collapses with a “slower” change of driving pressure, the split structures are not propagated as closely to the wall and the resulting pressure impact is therefore lower.

4. CFD investigation of hydrodynamic cavitation in Venturi tube

4.1 Simulation model and methodology

The simulations of cavitation flow in the Venturi nozzle corresponding to the previous presented results from experimental measurements are presented. First, the viability of three different turbulence models (SST $k-\omega$, SST $k-\omega$ with modified turbulent viscosity and SBES) is assessed on a limited number of σ configurations. Based on this study, the whole range of σ is analysed with the SBES turbulence model. The cavitation structures are compared with recordings from a high-speed camera. The loss coefficients, shedding frequency and the magnitude of the pressure waves are also compared.

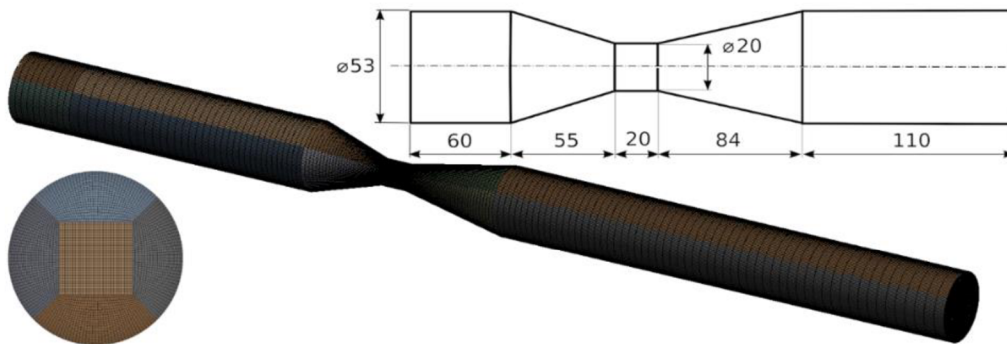


Figure 20 - Dimensions of the Venturi nozzle; computational domain with cross-section detail

The current work analyses the shedding mechanism within 3-D geometry instead of frequently used simplified 2-D axisymmetric geometries. The dimensions of the Venturi nozzle can be seen in Figure 20. The domain spatial discretization is done by full structural hexahedral mesh. The cell size is 950 000 cells with the size of 0,28 mm in the centre of the throat area. The mesh as well as cross-section detail can also be seen in Figure 20. The simulation is done with adaptive time stepping to accurately capture the collapse of cavitation structures while maintaining a reasonably high time step. The stability requirements of the time-integration scheme are defined by the Courant-Friedrichs-Lewy (CFL). The targeted CFL is 2 which corresponds to timestep around $1 \cdot 10^{-6}$.

As for the solution schemes the following schemes are used for the SBES: Coupled pressure-velocity coupling, PRESTO! pressure scheme, Bounded Central Differencing Momentum scheme, Bounded Second Order Implicit Transient scheme and First Order Upwind scheme for the density, volume fraction, turbulent kinetic energy, specific dissipation rate and energy. The SST variants use Second Order Upwind for the Momentum scheme. The implicit Homogenous Mixture model with a Dispersed Interface Model is used with a constant bubble diameter of $1 \cdot 10^{-5}$ m. As for the forces acting on the secondary phase, the Continuum Surface Force model

with a surface tension coefficient of 0.072 N/m and the Schiller-Naumann model for the drag force are used. The Schnerr-Sauer cavitation model is used with a vapor pressure of 3540 Pa and bubble number density of $1 \cdot 10^{11}$. Both vapor and liquid are assumed as compressible to accurately capture resulting pressure waves. The mass flow rate inlet boundary is used and the cavitation number is regulated by pressure outlet.

4.2 Results of the CFD investigation

In Figure 21, we can see the comparison of one shedding cycle of the volume fraction iso-surface ($\alpha = 0.1$) for SST, modSST and SBES turbulence models and high-speed camera recording for $\sigma = 0.5$. Both the modSST and SBES turbulence models are able to capture the shedding cycle fairly well. We can see inception on the leading and trailing edge of the Venturi nozzle followed by connection of these two structures and further extension to the diffuser. After the collapse of the previous cavitation structure, the shedding due to resulting pressure wave can be observed and further decay of the structure up until the leading edge of the nozzle.

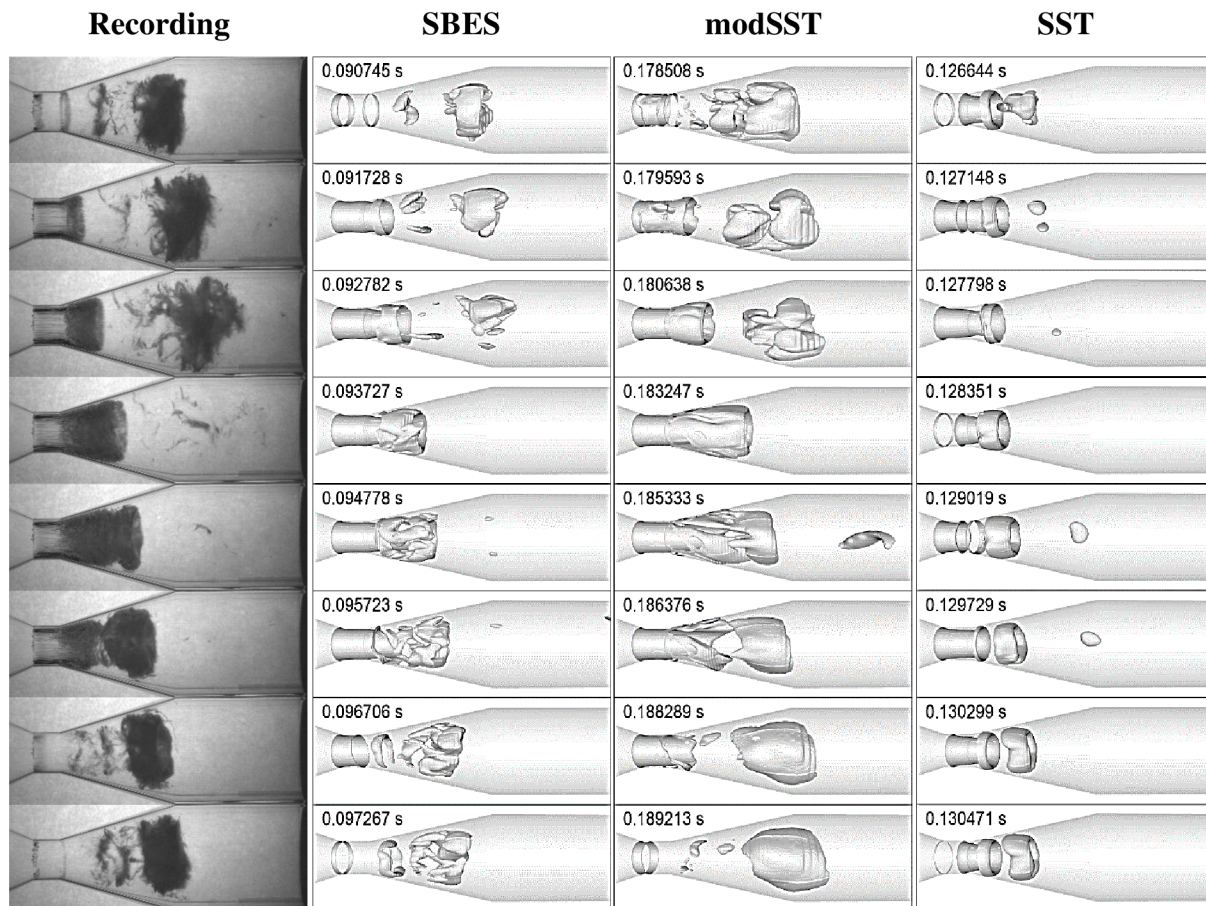


Figure 21 – Comparison of volume fraction iso-surface ($\alpha = 0.1$) of SST, modSST and SBES turbulence models ($\sigma = 0.5$) and high-speed camera recording ($\sigma = 0.518$) for (one shedding cycle).

Generally, the length of the structure before shedding is overpredicted slightly by the modSST model and the structures are more uniform with less small secondary structures. The unmodified SST on the other hand fails to predict the collapse as the bubble clouds shed more frequently and therefore are not large enough to produce sufficient pressure wave to decay the entire cavitation structure. The shedding cycle resembles transition from initial to partial cavitation that can be observed for higher values of σ .

In Figure 22, we can see the contours of velocity magnitude and static pressure during the same shedding cycle for the SBES model. From the velocity contours, the progress of shedding around the walls can be studied. We can see the reversed flow in the vicinity of the wall that initiates the shedding process. As for the static pressure contour, the 4th image depicts the pressure wave created by the cavitation collapse of previously shed cloud. The magnitude of the pressure collapse reaches 1.17 MPa.

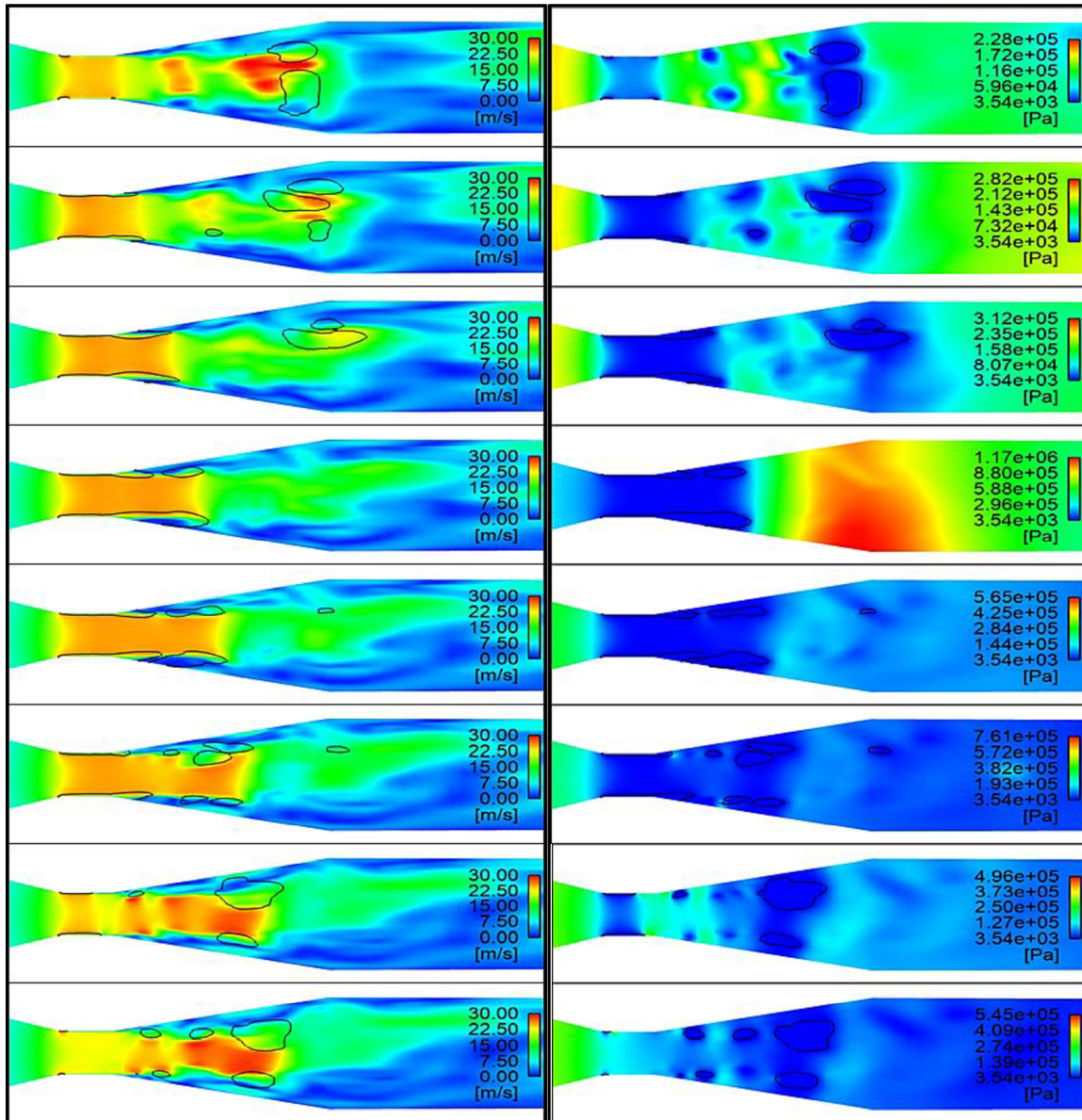


Figure 22 – Left: Contours of velocity magnitude; right: Contours of static pressure (SBES, $\sigma = 0.5$, one shedding cycle).

In Figure 23, we can see the comparison of loss coefficients and dominant frequencies between experimental measurements and the CFD simulations with SBES for the whole range of σ . The loss coefficients are in good agreement with each other and we can observe a typical linear increase of loss coefficient with decreasing σ . The dominant frequencies of emerging pressure waves are in good agreement with frequencies captured by the pressure sensors for most of the fully developed region up until $\sigma = 0.5$ where the cavitation flow starts to transition to the partial cavitation and eventually to the initial cavitation. For $\sigma = 0.6$ and 0.7 , the dominant frequency is 167 Hz and 195 Hz, while the experimentally observed dominant frequency is 107 and

158 Hz, respectively. Even larger discrepancy can be observed for $\sigma = 0.8$ and 0.9 where frequencies are 670 and 750 Hz, while 175 and 138 Hz are obtained from experimental measurements. It should be noted that proper assessment of the frequencies is problematic for $\sigma = 0.7, 0.8, 0.9$ as the results from FFT analysis are too noisy and therefore the frequency is estimated from the pressure signal. This is also true for the $\sigma = 0.6$, but for this configuration, the cycle can be determined from the images of pressure contours.

On the contrary, the dominant frequencies from the velocity monitor are in agreement with the measurement for all cavitation regions which indicates that unphysical pressure waves are appearing in the computational domain that skew the monitored frequencies. During the cavitation collapse the pressure waves are reflected on the inlet and outlet of the computational domain and propagate once again towards the Venturi nozzle. The reflecting pressure waves also create regions of low pressure which creates unphysical cavitation structures that immediately collapse and thus create another pressure wave.

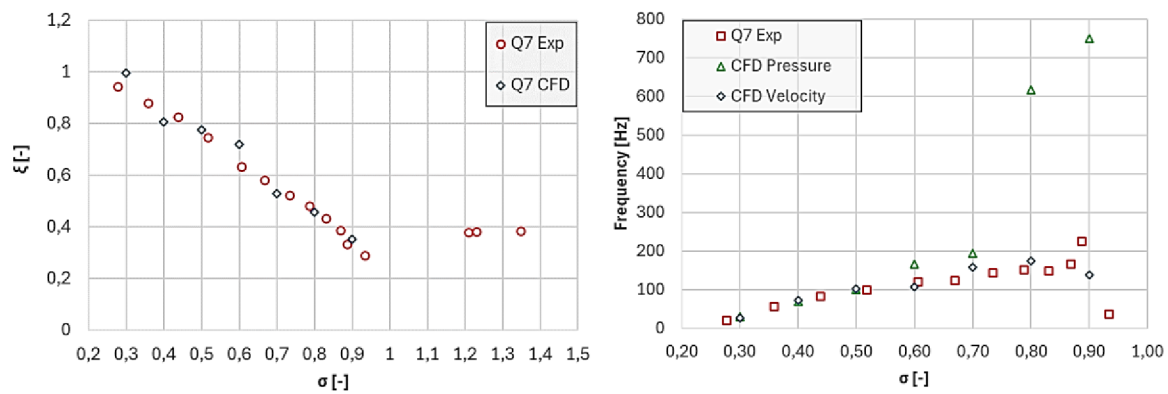


Figure 23 - Comparison of loss coefficient (left) and dominant shedding frequency (right) between CFD simulations and experimental measurement.

To properly resolve the pressure wave oscillations, the computational setup has to be adjusted to dampen the pressure wave reflections. The reflection on inlet boundary condition can be dampened by the porous medium. The outlet boundary condition can be improved by extending the computational domain. The domain is extended 1000 mm at the outlet while the inlet extension is kept at 130 mm. The rest of the meshing setup remains the same to ensure comparable spatial discretization to the previous simulation case. The resulting mesh consists of approximately 1 300 000 cells with a size of 0.28 mm in the centre of the throat area. The simulation is performed for $Q = 7$ l/s and $\sigma = 0.5, 0.7$ and 0.9 to assess the improvement over previous simulations case in problematic cavitation regions.

Figure 24 details the comparison of the averaged rolling maximum of pressure peaks and dominant frequencies between CFD simulations and experimental measurement. The extension of the computational domain provided enough damping of the emerging pressure waves that the reflections on boundary conditions is no longer present. The averaged magnitude of pressure waves for $\sigma = 0.5$ is 525 kPa and is in good agreement with experimental measurement ($\sigma = 0.517$; $p = 501$ kPa). The value for $\sigma = 0.7$ is 303 kPa which is slightly overpredicted in comparison with the averaged magnitude of 225 kPa obtained from linear regression of two closest points ($\sigma = 0.735$ and 0.668). The averaged magnitude for $\sigma = 0.9$ is 12 kPa which is underpredicted when compared to the closest measured point ($\sigma = 0.887$; $p = 31.8$ kPa).

As for the frequency of the pressure waves, the frequency for $\sigma = 0.5$ drops slightly from 100 Hz to 95 Hz, still in good agreement with the experiment. On the contrary, the frequency for $\sigma = 0.7$ is 63 Hz, which is two times lower than the expected value. As for the $\sigma = 0.9$, the dominant frequency is 173 Hz which follows the trend from the experiment, though it should be stressed that proper evaluation of initial cavitation is problematic even for experimental measurement and is also heavily affected by the defects on the Venturi nozzle. Nevertheless, it still provides major improvement from the previous simulation case, both in terms of frequency and magnitude of pressure fluctuations.

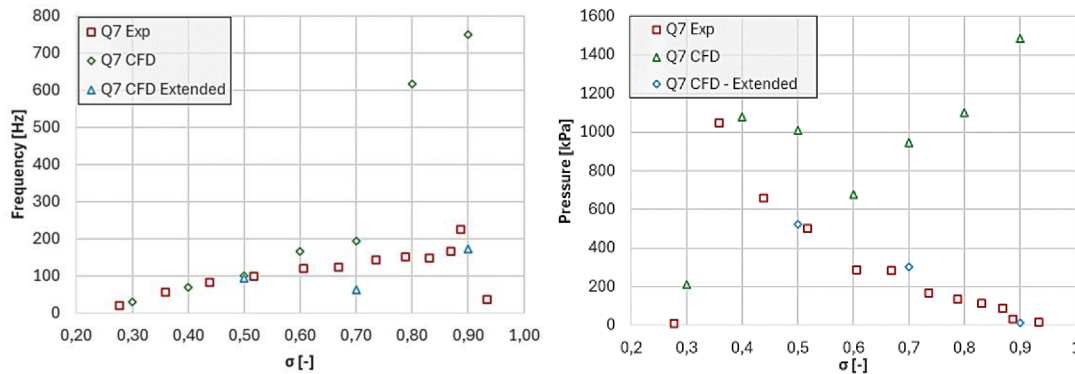


Figure 24 - Comparison of averaged rolling maximum of pressure peaks (left) and dominant frequency from pressure monitor (right) between CFD simulations and experimental measurement.

Conclusion

The main objective of this doctoral thesis is to investigate the interaction of the cavitation structures with the unsteady pressure field induced by the cavitation collapse by means of numerical simulations and experimental measurements.

A major effort is focused on providing comprehensive state of the art research on different modelling approaches, mainly in terms of appropriate multiphase, mass transfer and turbulence models. This research underlines the necessity of different modelling approaches for different types of cavitation flow, which indicates that numerical simulations including all cavitation length scales are too complex to investigate. Therefore, the problem is reduced to simplified case studies – the single bubble collapse near a solid wall and the hydrodynamic cavitation in the converging-diverging Venturi nozzle.

The results for the cavitation collapse of a single bubble near a solid wall highlight the influence of three main parameters - the stand-off distance γ , the driving pressure p_d and the duration of the step-function t_s . The most significant impact is connected to the stand-off distance γ , where not only the magnitude but also the overall nature of the collapse is influenced. With a high value of γ , only one pressure peak appears on the solid wall as the pressure waves from jet penetration and bubble collapse coincide with each other and no additional splitting of the main bubble takes place. For closer positions of the bubble to the wall, the 4 main impacts are present – from jet impact, main bubble collapse and collapse of second and third split bubble structures. The first bubble structure does not collapse during the first stage and is propagated outwards of the axis. With decreasing γ , the magnitude of the impacts rapidly increases as the bubble is closer to the solid wall therefore the pressure waves are less dampened by the surrounding liquid. Also, the velocity during the jet penetration can reach super-sonic speed and the velocity generally increases with increasing γ due to the change in sphericity of the bubble.



The driving pressure p_d heavily influences the magnitude of the impacts but does not change the overall nature of the collapse. The duration of the step-function t_s also influences the magnitude of the impacts and decreases the significance of split bubble structures as they are less propagated to the solid wall and therefore the impact is more dampened by the surrounding liquid.

The results from the second simulation case – hydrodynamic cavitation in Venturi nozzle – show that an axial Venturi nozzle is significantly influenced by turbulence. The SST model proves inadequate for analysing the shedding dynamics. In contrast, both the SBES and modified SST models can accurately resolve the shedding frequencies and the characteristics of cavitation structures, showing results comparable to the experiment. However, these models differ in the amplitude of the resulting pressure fluctuations and therefore SBES turbulence model is utilized to further analyse the entire range of σ configurations.

While the SBES turbulence model successfully predicts the loss coefficient across the entire range of cavitation numbers, it struggles to accurately capture the resulting pressure waves due to reflections from the boundary conditions and subsequent collapses of unphysical cavitation structures, mostly in the regions of initial and partial cavitation, while the fully developed cavitation region is modelled sufficiently. Therefore, the computational domain was extended, which proved to effectively dampen the reflection of pressure waves from cavitation collapse, significantly improving the robustness of the simulation. Unfortunately, while the modification improved the accuracy of capturing the pressure wave magnitudes, particularly in the region of partial cavitation, the frequency and shape of the cavitation structures in this region still differ from the experimental measurements, most likely due to defects on the leading edge of the Venturi nozzle.

The numerical simulations are complemented with experimental measurements conducted in the hydraulic laboratory of Viktor Kaplan Dept. of Fluid Engineering to capture the behaviour of cavitation structures in a converging-diverging Venturi nozzle. The interaction of cavitation structures and emerging pressure waves in the Venturi nozzle is investigated via high-speed camera recording and transducers of static pressure, dynamic pressure, radial and axial acceleration, and acoustic emission.

Analysis of pixel intensities is used to determine the distribution of cavitation vapor and to create the x-t diagrams, which help identify the region of the re-entrant jet and bubbly-shock dominant mechanism region. From the results, it is apparent that the bubbly-shock mechanism is dominant on most of the σ . Additionally, FFT analysis is performed to determine the dominant frequencies corresponding to the time signals of mean pixel intensities. Results for all flow rates follow the same pattern of decreasing dominant frequency with a decreasing value of σ . The investigation is unfortunately limited by the lower frame rate of the high-speed camera.

In the second part of the chapter, the POD of high-speed images is used to decompose the complex cavitation phenomenon into temporal and spatial modes to identify and investigate the most dominant instabilities. The 1st mode (the most impactful dynamic mode) is mostly non-dependant on the cavitation number as the most energy is contained in the axial pulsation of the cavitation cloud for most of the σ range. On the contrary, the most dominant “switching” frequency between shedding mechanisms can be determined in the transition region. This is also confirmed by the x-t diagrams. The importance of the “switching” frequency is highest in



the middle of the transition region and decreases once one of the shedding mechanisms is prevalent.

Lastly, dynamic and time-averaged data acquired from various transducers are studied to further analyse the dynamics of the cavitation structures, the loss coefficients, average and maximum values of measured pressure peaks and frequencies from the FFT. The pressure pulses do not increase linearly up until the transition to super-cavitation, but similarly to radial pulsations decrease slightly with the transition from partial to fully developed cavitation and increase again up until the transition to super-cavitation. From the absolute values of RMS, we can also detect non-linear increase with increasing flow rate. The results from the FFT analysis show a linear decrease in frequency with decreasing σ for all flow rates. The flow rates impact the transition region where the switch from the bubbly-shock mechanism occurs quicker with an increasing flow rate.

From the comparison between x-t diagrams, POD and the analysis of data from transducers, we can see that the results from all methods are in agreement for the whole cavitation range. The x-t diagram is unable to provide any additional information like the re-entrant jet frequency and the “switching” frequency between the mechanisms. The POD method is the only one that provides the shape of the connected dynamic phenomena. The benefit of determination from the pressure signal is that the super-cavitation region can be studied as well, whereas no relevant data can be used from the high-speed camera record of the Venturi nozzle as the region appears to be stable.

As for the recommendations for future research, the most interesting improvement to the numerical models can be acquired by combining multiphase approaches together to create a hybrid model which is able to couple two or more approaches to accurately capture different length-scale of the cavitating flow as realistically as possible. As highlighted during the single bubble collapse simulation case, the positions and interactions between collapsing cloud-forming bubbles play an important part in the character of the collapse. However, the homogenous mixture model, utilized for hydrodynamic cavitation, does not take this fact into consideration and thus cannot accurately predict the nature of the collapse and subsequent pressure waves. While the testing of the VoF method for sheet cavitation in combination with DPM to track the position of individual bubbles proved to be far too unstable, a similar approach in combination with a homogeneous mixture model could yield a more promising result.

Lastly and most importantly, the simulation case of single bubble collapse can be repeated with the inclusion of chemical reactions to assess the effect of micro-scale collapses on the chemical bonds of biological and chemical contaminants, especially in synergy with cold plasma discharge in the CaviPlasma device [27]. This way, the simulation model can be utilized to not only predict the influence of geometry changes of the device on the characteristics and dynamics of the cavitation cloud, but also its potential of removing different pollutants.

References

- [1] FRANC, Jean-Pierre; MICHEL, Jean-Marie. Fundamentals of cavitation. Springer science & Business media, 2006.
- [2] ARNDT, Roger EA. Cavitation in fluid machinery and hydraulic structures. Annual Review of Fluid Mechanics, 1981, 13.1: 273-326.
- [3] ESCALER, Xavier, et al. Detection of cavitation in hydraulic turbines. Mechanical systems and signal processing, 2006, 20.4: 983-1007.
- [4] GAVAISES, M., et al. Link between cavitation development and erosion damage in diesel injector nozzles. SAE Technical Paper, 2007.
- [5] GIANNADAKIS, E.; GAVAISES, M.; ARCOUMANIS, C. Modelling of cavitation in diesel injector nozzles. Journal of Fluid Mechanics, 2008, 616: 153-193.
- [6] RAMBOD, Edmond, et al. A physical model describing the mechanism for formation of gas microbubbles in patients with mitral mechanical heart valves. 1999.
- [7] JAKOBSEN, Jakob K.; KELLER JR, R. B. Liquid rocket engine turbopump inducers. 1971.
- [8] YU, Tinghe; WANG, Zhibiao; MASON, Timothy J. A review of research into the uses of low-level ultrasound in cancer therapy. Ultrasonics sonochemistry, 2004, 11.2: 95-103.
- [9] COLEMAN, Andrew J., et al. Acoustic cavitation generated by an extracorporeal shockwave lithotripter. Ultrasound in medicine & biology, 1987, 13.2: 69-76.
- [10] BRENNEN, Christopher Earls. Cavitation in medicine. Interface focus, 2015, 5.5: 20150022.
- [11] VOGEL, Alfred. Nonlinear absorption: intraocular microsurgery and laser lithotripsy. Physics in Medicine & Biology, 1997, 42.5: 895.
- [12] GEDANKEN, Aharon. Using sonochemistry for the fabrication of nanomaterials. Ultrasonics sonochemistry, 2004, 11.2: 47-55.
- [13] OHL, Claus-Dieter, et al. Surface cleaning from laser-induced cavitation bubbles. Applied physics letters, 2006, 89.7: 074102.
- [14] SUN, Xun, et al. A review on hydrodynamic cavitation disinfection: The current state of knowledge. Science of the Total Environment, 2020, 737: 139606.
- [15] SUPPONEN, Outi. Collapse phenomena of deformed cavitation bubbles. EPFL, 2017.
- [16] RUDOLF P., HUDEC M., GRÍGER M., ŠTEFAN D., Characterization of the cavitating flow in converging-diverging nozzle based on experimental investigations, 2014.
- [17] HIRT, Cyril W.; NICHOLS, Billy D. Volume of fluid (VOF) method for the dynamics of free boundaries. Journal of computational physics, 1981, 39.1: 201-225.



- [18] Ansys® Ansys Fluent, Release 21.2, Help System, ANSYS Fluent Theory Guide, Basic Fluid Flow, ANSYS, Inc; 14.3.4. Volume Fraction Equation.
- [19] MA, Jingsen; HSIAO, Chao-Tsung; CHAHINE, Georges L. A physics based multiscale modeling of cavitating flows. *Computers & fluids*, 2017, 145: 68-84.
- [20] GENG, Linlin. Numerical investigation and modelling of the unsteady behavior and erosion power of cloud cavitation. 2021.
- [21] SCHNERR, Günter H.; SAUER, Jürgen. Physical and numerical modeling of unsteady cavitation dynamics. In: *Fourth international conference on multiphase flow.*, 2001.
- [22] AGUADO, Pablo. Etude numérique de l'impact de la géométrie de la buse de l'injecteur sur l'écoulement à l'intérieur de la buse et l'atomisation primaire. 2017. PhD Thesis.
- [23] COUTIER-DELGOSHA, Olivier; FORTES-PATELLA, Regiane; REBOUD Evaluation of the turbulence model influence on the numerical simulations of unsteady cavitation. 2003
- [24] MENTER, Florian. Stress-blended eddy simulation (SBES)—A new paradigm in hybrid RANS-LES modeling. In: *Progress in Hybrid RANS-LES Modelling: 2016*, Strasbourg, 2018.
- [25] XU, Shuangjie, et al. Experimental study of the cavitation noise and vibration induced by the choked flow in a Venturi reactor. *Ultrasonics Sonochemistry*, 2020, 67: 105183.
- [26] HSIAO, Chao-Tsung, et al. Modelling of material pitting from cavitation bubble collapse. *Journal of Fluid Mechanics*, 2014, 755: 142-175.
- [27] Rudolf, P.; Pochylý, F.; Sťahel, P.; Ráhel, J.; Čech, J.; Maršálek, B. Apparatus for purifying liquids and a method for purifying liquids using this apparatus. Czech Patent No. 308532, 2019.

Curriculum Vitae

Ing. Radim Burda

21. 3. 1995, Brno, Czech Republic



EDUCATION

- 2019 – 2024 *Brno University of Technology, Faculty of Mechanical Engineering. Specialisation: Fluid Engineering, Doctoral study. Theme: Cavitation collapse induced by unsteady pressure field*
- 2017 – 2019 *Brno University of Technology, Faculty of Mechanical Engineering. Programme: Fluid Engineering, Master's programme.*
- 2014 – 2017 *Brno University of Technology, Faculty of Mechanical Engineering. Programme: Engineering, Bc. Programme.*

EMPLOYMENT

1. SVS FEM s.r.o.

2019 – present *CFD engineer*